Journal Pre-proof

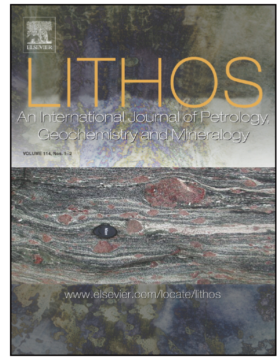

Identifying deep recycled carbonates through Miocene basalts in the Maguan area, SE Tibetan Plateau

Hangshan Lei, Zhidan Zhao, Yaoling Niu, Shuangquan Zhang, Brian Cousens, Qian Ma, Fang-Zhen Teng, Dong Liu, Zhuang Miao, Yiyun Yang, Jingkai Wu, Qing Wang, Di-Cheng Zhu

PII: S0024-4937(21)00392-3

DOI: https://doi.org/10.1016/j.lithos.2021.106356

Reference: LITHOS 106356

To appear in: *LITHOS*

Received date: 4 March 2021

Revised date: 8 July 2021

Accepted date: 8 July 2021

Please cite this article as: H. Lei, Z. Zhao, Y. Niu, et al., Identifying deep recycled carbonates through Miocene basalts in the Maguan area, SE Tibetan Plateau, *LITHOS* (2021), https://doi.org/10.1016/j.lithos.2021.106356

Identifying deep recycled carbonates through Miocene basalts in the Maguan area, SE Tibetan Plateau

Hangshan Lei[a,b], Zhidan Zhao[a,*], Yaoling Niu[a,c,d,e], Shuangquan Zhang[b], Brian Cousens[b], Qian Ma[a], Fang-Zhen Teng[f], Dong Liu[a], Zhuang Miao[a], Yiyun Yang[a], Jingkai Wu[a], Qing Wang[a], and Di-Cheng Zhu[a]

[a] *State Key Laboratory of Geological Processes and Mineral Resources, and School of Earth Science and Mineral Resources, China University of Geosciences, Beijing 100083, China.*

[b] *Isotope Geochemistry and Geochronology Research Centre, Department of Earth Sciences, Carleton University, Ottawa, ON K1S 5B6, Canada*

[c] *Laboratory for Marine Geology, Qingdao National Laboratory for Marine Science and Technology Qingdao 266061, China*

[d] *Department of Earth Sciences, Durham University, Durham DH1 3LE, UK*

[e] *Institute of Oceanology, Chinese Academy of Sciences, Qingdao 266071, China*

[f] *Isotope Laboratory, Department of Earth and Space Sciences, University of Washington, Seattle, WA 98195-1310, USA*

Manuscript submitted to Lithos

Corresponding author at:

Zhidan Zhao

State Key Laboratory of Geological Processes and Mineral Resources, and School of Earth Science and Resources, China University of Geosciences, Beijing 100083, China.

Tel: +86-10-82321115

E-mail: zdzhao@cugb.edu.cn

Identifying deep recycled carbonates through Miocene basalts in the Maguan area, SE Tibetan Plateau

Hangshan Lei[a,b], Zhidan Zhao[a,*], Yaoling Niu[a,c,d,e], Shuangquan Zhang[b], Brian Cousens[b], Qian Ma[a], Fang-Zhen Teng[f], Dong Liu[a], Zhuang Miao[a], Yiyun Yang[a], Jingkai Wu[a], Qing Wang[a], and Di-Cheng Zhu[a]

[a] *State Key Laboratory of Geological Processes and Mineral Resources, and School of Earth Science and Mineral Resources, China University of Geosciences, Beijing 100083, China.*

[b] *Isotope Geochemistry and Geochronology Research Centre, Department of Earth Sciences, Carleton University, Ottawa, ON K1S 5B6, Canada*

[c] *Laboratory for Marine Geology, Qingdao National Laboratory for Marine Science and Technology Qingdao 266061, China*

[d] *Department of Earth Sciences, Durham University, Durham DH1 3LE, UK*

[e] *Institute of Oceanology, Chinese Academy of Sciences, Qingdao 266071, China*

[f] *Isotope Laboratory, Department of Earth and Space Sciences, University of Washington, Seattle, WA 98195-1310, USA*

Manuscript submitted to Lithos

Corresponding author at:

Zhidan Zhao

State Key Laboratory of Geological Processes and Mineral Resources, and School of Earth Science and Resources, China University of Geosciences, Beijing 100083, China.

Tel: +86-10-82321115

E-mail: zdzhao@cugb.edu.cn

Abstract

Cenozoic mantle-derived magmas are widespread on the Tibetan Plateau, and provide evidence for the evolution of deep mantle and its influence on the Plateau development. Miocene basalts in the Maguan area on the southeastern Plateau have high MgO (9.13-13.10 wt.%) and $Mg^{\#}$ (0.60-0.70) with high Ce/Pb (10.6-32.5) and Nb/U (43.7-52.9) ratios, similar to those of oceanic basalts. Distinct from Eocene-Oligocene mantle-derived potassic magmas in Western Yunnan and Cenozoic basic volcanic rocks in Tengchong, these Maguan basalts are characterized by high large ion lithophile elements (LILEs) concentrations, positive anomaly in high field strength elements (HFSEs) and depleted Sr-Nd isotopes, consistent with the melt of an asthenospheric mantle origin. The high Ce/Pb and Nb/Y (1.80-2.68) ratios together with low Ba/Y and Ba/Th ratios indicate a significant input of slab-derived melt into the asthenospheric source. Besides, Hf/Hf* and Ti/Ti* ratios are significantly lower than those of ocean island basalt (OIB), which are proportional to the lighter $\delta^{26}Mg$ (-0.40--0.60 ‰) values. Based on the results of experimental petrology, the Sr-Mg isotope mixing model suggests that the asthenospheric mantle beneath the Maguan area had undergone the significant metasomatism of recycled carbonates prior to the late Miocene. The above petrological and geochemical understanding, together with the geophysical data, allows us to propose that the mantle metasomatism is most probably associated with the Neo-Tethys seafloor subduction, which is further testified by the decoupling between depleted Sr-Nd isotopes and elevated LILE concentrations.

Keywords: the Tibetan Plateau; Cenozoic magmatism; Sr-Nd-Mg isotopes; Asthenosphere; Metasomatism

1. Introduction

Since the Indian plate initially collided with the Eurasian plate in the early Paleogene (e.g., Jaeger et al., 1989; Rowley, 1996), mantle-derived magmatism has been widespread throughout the Tibetan Plateau (e.g., Ding et al., 2003; Chung et al., 2005; Huang et al., 2010; Tian et al., 2017). The magmatism offers a lithosprobe into the composition and evolution of the deep mantle, which further provides evidence on the Plateau development (e.g., Wang et al., 2001; Guo et al., 2005; Zhao et al., 2009; Liu et al., 2015; Tian et al., 2017). After the India-Asia continental collision, mantle-derived magmatism initiated in the Lhasa terrane (i.e., Linzizong volcanic suites), and migrated outward to the Qiangtang terrane in the north, western Qinling region in the northeast and Sanjiang tectonic belt in the southeast, which was dominated by magmas of K-rich composition (e.g., Ding et al., 2003; Chung et al., 2005; Mo et al., 2006). Normally, these K-rich magmas are characterized by the enrichment in large ion lithophile elements (LILEs) and light rare earth elements (LREEs), but depleted in high field strength elements (HFSEs) with enriched Sr-Nd isotopes. And it has reached a consensus that these K-rich magmas were derived from partial melting of metasomatically enriched lithospheric mantle although some details of mantle dynamics remain under debate (e.g., Wang et al., 2001; Zhao et al., 2009; Huang et al., 2010; Tian et al., 2017).

In comparison, there have been few cases on magmas of asthenospheric origin throughout the Plateau although a wealth of studies, especially seismic tomography, have pointed to the dynamic significance of asthenosphere in causing lithospheric mantle melting (e.g., Ding et al., 2003; Chung et al., 2005; Zhou and Lei, 2016; Tian et al., 2017). With the India-Asia continental collision and subsequent magmatism migration, it has become curious how the asthenosphere beneath the Tibetan Plateau may have been evolved. Previous studies have argued that Miocene basalts in the Maguan area, southeastern Tibetan Plateau (the SE Plateau, Fig. 1a) may be of asthenospheric origin (e.g., Wang et al., 2001; Xia and Xu, 2005; Flower et al., 2013; Liu et al., 2020). We thus choose these basalts as a window to study the evolution of the asthenospheric mantle beneath the Tibetan Plateau. Wang et al. (2001) considered that the mantle source beneath the Maguan area had been enriched by recent mantle metasomatism, and the magmatic event was caused by east-west extension throughout east Asia. However, Xia and Xu (2005) argued that the opening of the South China Sea may be responsible for the Miocene magmatism in the Maguan area. Furthermore, Flower et al. (2013) suggested that tectonic extension associated with the “tectonic escape” and anomalous mantle potential temperature both have played some roles in causing the mantle melting. Based on Mg-Zn isotopes, the latest study further suggested that the recycled Zn-rich magnesium carbonates were recorded in the source of the Maguan basalts (Liu et al., 2020). In order to help resolve the heated debate, we carried out a study and present here bulk-rock geochemical and Sr-Nd-Mg isotopic data, to delineate mantle enrichment and related evolution of asthenosphere beneath the SE Plateau.

2. Geological background and sampling

The study area, Maguan, is situated at the southeastern margin of the Tibetan Plateau, occupying the southwestern corner of the South China block (Fig. 1a). And the well-known Ailaoshan-Red River shear zone (RRSZ) is on the west side of the Maguan area, and extends over 1000 km from the SE Plateau to the South China Sea. In the response to the India-Asia continental collision, RRSZ underwent significant left-lateral shearing at ~30-17 Ma (e.g., Gilley et al., 2003) and extruded the Indochina block to the SE by ~500-700 km (e.g., Tapponnier et al., 1990; Chung et al., 1997).

Magmatic activities in the Maguan area commenced intermittently from the late Paleozoic to Neogene, represented by (1) the late Paleozoic diabases with minor gabbros, (2) Cretaceous granitoids, and (3) Miocene alkali basalts with explosive breccias (Wang et al., 2001; Xia and Xu, 2005; Huang, 2012). The youngest magmatism in the Maguan area distributes from the Bazhai area to Muchang village, cropping out an area of ~8 km^2 (Fig. 1b). Geological survey has identified ~40 dykes or pipes, including Laofangzi, Zhenjiashan, Haoziba and Xiahetou pipe (Fig. 2a). These magmas prevailingly erupted and intruded into Cambrian-Ordovician strata constrained by both northwest-trending and northeast-trending fold systems. The rock assemblage is dominated by olivine basalts with localized explosive breccias associated with volcanic constructs. The olivine basalts also host mantle xenoliths (mainly spinel lherzolite) of up to 30 cm in size. A ^{40}Ar-^{39}Ar dating on the basalt groundmass yielded an eruption age of 13.3-11.7 Ma, which is consistent with ^{40}Ar-^{39}Ar age on biotite of the related intrusive (12.4-11.9 Ma) (Wang et al., 2001; Huang, 2012).

Fifteen samples of basalts were collected from Haoziba, Zhenjiashan, Laochang, and Laofangzi pipe (Fig. 1b). Most of them are fresh, but Samples LFZ1614 and HZ1606 are visibly altered. The rest samples are mainly olivine basalts with porphyritic texture. Representative field photo and photomicrographs of these samples are given in Fig. 2. The petrography of all samples is quite similar (Fig. 2b-d): (1) The phenocryst assemblage is less than 15% by volume, and dominantly composed of olivine, clinopyroxene and plagioclase; (2) The groundmass displays intergranular texture, consisting of plagioclase, clinopyroxene, and olivine plus Fe-Ti oxides and minor glasses.

3. Analytical methods

3.1. Bulk-rock major and trace elements

Small pieces of fresh basalts without xenoliths selected by hand-picking were grinded to 200 mesh in an agate mortar. Major elements were analyzed in the State Key Laboratory of Geological Processes and Mineral Resources (GPMR), China University of Geosciences, Beijing. Rock powder (~0.03 g) was mixed with ~0.15 g $Li_2B_4O_7$ and fused in a Pt-Au crucible at ~1000 °C. After cooling down, the quenched glass was further dissolved by a mixture of 5% HNO_3. The final solution was diluted to ~60 mg with deionized water in a polyethylene bottle for ICP-OES (Prodigy) analysis. And the standard deviation is better than 5%.

Trace elements of bulk-rock rocks were analyzed by inductively coupled plasma mass spectrometry (Agilent 7700e ICP-MS) in Wuhan SampleSolution Analytical Technology Co., Ld, Wuhan. And the analytical precision and accuracy are less than 10%. Rock powders were weighted at 50 mg and dissolved by 1 ml HNO_3 and 1 ml HF in Teflon bombs. Then, the sealed bombs were heated at 190 ℃ for 24 hours at least. After evaporating and drying the solution, 1 ml HNO_3 was added in the bombs and dried again. After the addition of 1 ml HNO_3 + 1 ml MQ water + 1 ml In (internal standard), the sealed bombs were placed in the oven at 190 ℃ for more than 12 hours. The prepared solution was then transferred to a polyethylene bottle and diluted to 100 g by adding 2% HNO_3.

3.2. Bulk-rock Sr and Nd isotopes

Sr and Nd isotopes of bulk-rock samples were analyzed in the State Key Laboratory of Geological Processes and Mineral Resources (GPMR), China University of Geosciences, Beijing. Details of the analytical procedures are as follows: (1) Rock powders weighted at 500-100 mg and were dissolved by HF-HNO_3-HCl in Teflon bombs. (2) After the solution got dried by heating, HCl was added to dissolve the resultant salt in the bombs. (3) Rb, Sr, Sm, and Nd were separated and purified by Rb-Sr (AG50W-X12, 200-400 mesh) and Sm-Nd (LN resin) ion-exchange procedures, respectively. (4) The final solution was completed by adding 3% HNO_3 for MC-ICPMS (Thermo Scientific Neptune plus) analysis. The Sr standard (NBS987) and Nd standard (Alfa Nd) yielded $^{87}Sr/^{86}Sr$ = 0.710260 ± 28 (2SD, n=2) and $^{143}Nd/^{144}Nd$ = 0.512424 ± 1 (2SD, n=2), similar to the long-term measured values in the lab (NBS987 $^{87}Sr/^{86}Sr$: 0.710274 ± 21, 2σ, n=61; Alfa Nd $^{143}Nd/^{144}Nd$: 0.512423 ± 24, 2σ, n=58; Li et al., 2017). The results of monitored standard (BHVO-2) analysis were $^{87}Sr/^{86}Sr$ = 0.703508 ± 12 (2SD, n=3) and $^{143}Nd/^{144}Nd$ = 0.512964 ± 6 (2SD, n=3), consistent with the recommended reference values ($^{87}Sr/^{86}Sr$, 0.703480 ± 16; $^{143}Nd/^{144}Nd$, 0.512983 ± 10; Zhang and Hu, 2020).

3.3. Bulk-rock Mg isotopes

Mg isotopic compositions were analyzed by MC-ICPMS (Nu Plasma) at the Isotope Laboratory of the University of Washington, Seattle. Rock powders were weighed at 1-3 mg and were dissolved by HF-HNO_3- HCl in Teflon bombs. After drying the solution and cooling down, the anhydrous salt was dissolved again by 1 N HNO_3. To avoid the effects of matrix elements, the element of Mg was separated and purified by cation exchange resin (Bio-RadAG50W-X8, 200-400 mesh) twice. Details of the analytical methods and operating conditions for MC-ICPMS are given in Teng et al. (2010), (2015). Analysis of standards yielded δ^{26}Mg = -0.31 ± 0.06‰ (2SD) for JB-1 (basalt), δ^{26}Mg = -0.83 ± 0.01‰ (2SD, n=4) for seawater, which agree well with previously published results (JB-1: -0.276 ± 0.098‰; seawater: -0.83 ± 0.09‰; Teng et al., 2015)

4. Results

4.1. Bulk-rock major and trace element geochemistry

Bulk-rock major and trace element compositions are summarized in Table A.1. The loss on ignition (LOI) values are generally <4.2 wt.% except for the two mentioned samples (HZ1606 and LFZ1614) with alteration-like high LOI values (6.47 wt.% and 7.86 wt.%, respectively). To avoid the effects of alteration, these two samples are excluded in the following discussion. The LOI values of the rest thirteen samples do not give a significant correlation with Ba and $^{87}Sr/^{86}Sr$ ratios (Fig. A.1), revealing they are not significantly affected by alteration. It is noteworthy that in making major element plots, we recalculated the data to 100% on an anhydrous basis. The analyzed samples show a limited range of MgO (9.13-13.10 wt.%), Al_2O_3 (12.59-14.67 wt.%) and CaO (7.68-8.73 wt.%) contents (Fig. 3). Most samples show a high-K and shoshonitic affinity based on SiO_2, Na_2O and K_2O compositions (Fig. A.2).

The analyzed samples contain 321-486 ppm Ba, 56.7-123.7 ppm Rb, 447-945 ppm Sr, and are alkali basalts with low Zr/TiO_2 and relatively high Nb/Y (Fig. 4; Pearce, 1996). Besides, these samples are slightly enriched in LREEs (Fig. 5a) with high $(La/Yb)_N$ ratios (9.57-17.26, subscript "N" denotes normalization to chondrite values). On primitive mantle-normalized multi-element spider diagram (Fig. 5b), these basalts show enrichments in LILEs (e.g., Rb, Ba) with no significant negative anomalies in HFSEs (e.g., Nb, Ta), resembling average ocean island basalt

(OIB). In addition, there are no significant Eu anomalies in these samples (δEu = 0.95-0.99, δEu = 2×$(Eu)_N$ /[$(Sm)_N$ + $(Gd)_N$**]**.

4.2. Bulk-rock Sr-Nd isotopes

Sr-Nd isotopic compositions of the analyzed four basalts are given in Table A.2. Due to young ages of alkali basalts (ca. 13.3-11.7 Ma), Sr-Nd isotope data are not age-corrected. These basalts yield uniform $^{87}Sr/^{86}Sr$ ratios (0.70406-0.70440) and $\varepsilon_{Nd}(0)$ values (5.3-6.5), which plot outside of mid-ocean ridge basalt (MORB) field but within EM II-type OIB area (Fig. 6a). In the Sr-Nd isotope space (Fig. 6a), the Maguan alkali basalts are distinguished from Tengchong volcanic rocks and Eocene-Oligocene mantle-derived potassic magmas (ca. 42-24 Ma, Wang et al., 2001) in Western Yunnan which exhibit high $^{87}Sr/^{86}Sr$ ratios and low $\varepsilon_{Nd}(0)$.

4.3. Bulk-rock Mg isotopes

Mg isotopic compositions of the analyzed samples are given in Table A.2. These basalts plot along the terrestrial equilibrium mass fractionation line with a slope of 0.521 in $\delta^{25}Mg$ vs. $\delta^{26}Mg$ diagram (Fig. A.3, Young and Galy, 2004). They show a limited range of $\delta^{25}Mg$ (-0.32--0.18‰) and $\delta^{26}Mg$ (-0.60--0.40‰) values. Compared with global oceanic basalt ($\delta^{25}Mg$ = -0.13 ± 0.05‰, $\delta^{26}Mg$ = -0.26 ± 0.07‰, Teng et al., 2010) and the depleted MORB mantle (DMM, $\delta^{25}Mg$ = -0.13 ± 0.03‰, $\delta^{26}Mg$ = -0.25 ± 0.04‰, Teng et al., 2010), the Maguan alkali basalts have relatively lighter Mg isotopic compositions, similar to Tengchong volcanic rocks and Cenozoic basalts in Eastern China, but distinct from Eocene-Oligocene potassic magmas in Western Yunnan with DMM-like Mg isotopes (Fig. 6b).

5. Discussion

5.1. Magmatic processes

As indicated by the Miocene basaltic pipes (feeder dikes) in the Maguan area, the erupted basalts are expected to have undergone crustal contamination. Thus, it is necessary to assess the possible effect of crustal contamination. As summarized by O'Reilly and Griffin (2011), mantle xenoliths hosted in magmas take a maximum of 8-60 hours to reach the surface from the depth of 80-200 km. In the study area, mantle xenoliths are scattered in the Miocene pipes, with the maximum pressure of 2.93 GPa (~93 km, Yu et al., 2006), suggesting rapid ascent without enough time for crustal assimilation (Sun et al., 2018).

In addition, continental crustal material generally shows the features of high SiO_2 and low MgO contents, strongly enrichment in LILEs (e.g., Rb, Ba, U, and K), negative anomalies in HFSEs (e.g., Nb, Ta, and Ti), together with enriched Sr-Nd isotopic compositions, which are all lacking in the studied alkali basalts, pointing to the fact that crustal assimilation is rather insignificant if any. Therefore, addition of crustal material to the mantle melts would lead significant increase in SiO_2 and $^{87}Sr/^{86}Sr$, and decrease in MgO and $^{143}Nd/^{144}Nd$, but these are not observed. As shown in Fig. 3i, Sr isotopes are nearly constant with increasing MgO. Furthermore, Ce/Pb and Nb/U ratios in these basalts fall within the range of oceanic basalts (Ce/Pb = 25 ± 5, Nb/U = 47 ± 10; Hofmann et al., 1986), and are distinctly higher than average values expected for continental crust (4.8 and 7.4 respectively, Taylor, 1964). Also, there is no meaningful correlation between MgO contents and Ce/Pb or Nb/U ratios (Fig. 3g-h), indicating no significant crustal material input into these magmas. Hence, crustal contamination plays no significant role in the petrogenesis of these alkali basalts.

During xenolith-bearing melt ascent with cooling, crystallization can take place in a magma chamber developed in the lithospheric mantle (Sun et al., 2018). Clinopyroxene megacrysts hosted in the Maguan alkali basalts give equilibrium temperatures and pressures of 1152-1356 °C and 1.9-2.7 GPa, suggesting crystallization occurred under lithospheric mantle conditions (Li, 2009). Combined with the literature data, the varying major element compositional variation in MgO-variation diagrams (Fig. 3) with MgO as low as < 5.0 wt. % and the presence of phenocryst olivine and clinopyroxene are manifest for fractional crystallization of the Maguan alkali basalts (Fig. 2b-d). Therefore, we should note that the overall high MgO contents (9.60-13.10 wt.%), $Mg^{\#}$ (0.60-0.70) and Ni (225-415 ppm) in the studied bulk-rock compositions result from varying extent of phenocryst (olivine and clinopyroxene) contributions, and thus cannot be treated as primary melts. The lack of negative δEu negative anomalies (0.95-0.99) is consistent with the fact that plagioclase is not on the liquidus for most of these samples (Sun et al., 2018). Thus, olivine and clinopyroxene are the dominant liquidus phases of alkali basaltic magma evolution in the Maguan area.

Due to the incompatibility in olivine and clinopyroxene (Baudouin et al., 2020), the concentrations of incompatible elements in the Maguan basalts should be increased by the fractionation of olivine and clinopyroxene. Based on the fractional crystallization model by Ersoy and Helvacı (2010), the degree of fractional crystallization (Ol + Cpx) in the Maguan basalts could reach up to 50-60% (Fig. 7), inconsistent with the limited variations of CaO (7.68-8.73 wt.%) and MgO (9.13-13.10 wt.%). Besides, the concentrations of incompatible elements (e.g., Sr, LREEs) in the Maguan basalts are not correlated with MgO contents (Fig. A.4). Thus, it suggests that the variations of incompatible elements in the Maguan basalts cannot be simply explained by the process of fractional crystallization. Due to the differences of partition coefficients, the compositional differentiation among incompatible elements (e.g., La, Sm) would occur during the partial melting process (Allègre and Minster, 1978). In the Maguan basalts, ΣLREE, together with Sr, are positively proportional to $(La/Sm)_N$ ratios, which plot along the tendency of partial melting (Fig. 7). Therefore, in addition to the effect of fractional crystallization, the variations of incompatible elements in the Maguan basalts are also likely controlled by different degrees of partial melting.

5.2. Identifying the mantle source of the Maguan alkali basalts

Pearce (2008) shows that both OIB and MORB define a unique oblique array on Nb/Yb vs Th/Yb diagram with higher ratios for OIB (Fig. 8a). In contrast, volcanic arc rocks plot above the array with high Th/Nb ratios due to the low Nb content of slab-derived materials. Samples from the Maguan area plot on the MORB-OIB array with high Th/Yb (2.06-3.34) and Nb/Yb (26.27-45.81) (Fig. 8a). As the depth of melting increases, especially reaching the depth of spinel-garnet lherzolite transition zone, residual garnet begins to be involved and leads to extensive fractionation of TiO_2/Yb ratios at low degrees of melting because Yb is highly compatible in garnet relative to Ti (Pearce, 2008). Due to the different depths of melting (Niu, 2021), TiO_2/Yb ratio in MORB is significantly less than 0.8, evidently less than that of OIB (Fig. 8b; Pearce, 2008). Alkali basalts in this study have varying TiO_2/Yb (1.12-1.51) in the range of those as alkali OIB (Fig. 8b), consistent with the observations on trace-element patterns as illustrated in Chapter 4.1 (Fig. 5b). Moreover, MORB and OIB are characterized by depleted Sr-Nd isotopes (Fig. 6a) with N-MORB being more depleted with higher $^{143}Nd/^{144}Nd$ and lower $^{87}Sr/^{86}Sr$ ratios (Zindler and Hart, 1986). The Maguan alkali basalts of this study and the literature data (e.g., Wang et al., 2001; Xia and Xu, 2005; Huang, 2012) have homogeneous and slightly depleted Sr-Nd isotope compositions in the OIB field (Fig. 6a). As continental lithospheric mantle is suggested to not be the primary source of the OIB-type alkali magmatism which is akin isotopically and chemically to OIBs (e.g., Farmer, 2007), the aforementioned geochemical characteristics of the Maguan alkali basalts agree well with that of the OIB-type alkali magma, supporting the origin of sublithospheric mantle. Besides, during the Cenozoic period, the lithospheric mantle beneath the research field has been well recorded by Eocene-Oligocene potassic magmas in Western Yunnan, Tengchong volcanic rocks and hosted peridotite xenoliths in the Maguan basalts. The magmas in Western Yunnan and Tengchong are characterized by negative anomalies in HFSEs (e.g., Nb, Ta; Fig. 5b) and enriched Sr-Nd isotopic compositions (Fig. 6a), which were derived from enriched lithospheric mantle (e.g., Guo et al., 2005; Zhou et al., 2012). And Sr-Nd isotopic compositions of hosted peridotite xenoliths are similar to that of MORB (Fig. 6a), representing the depleted refractory lithospheric mantle (Huang, 2012). However, the geochemical records of lithospheric mantle mentioned above cannot explain the characteristics of the Maguan alkali basalts, excluding the possibility of lithospheric mantle origin. Additionally, the Maguan alkali basalts exhibit similar elemental and Sr-Nd-Mg isotopic geochemical characteristics to Cenozoic basalts in Eastern China (Fig. 5,6). As the basalts in Eastern China are produced by partial melting of asthenospheric mantle (e.g., Li et al., 2017), the Maguan alkali basalts are more likely derived from asthenospheric mantle, nor lithospheric mantle, which agrees well with the previous studies (e.g., Liu et al., 2020).

5.3. Geochemical fingerprints of mantle carbonate metasomatism

As several subduction events (e.g., a series of Tethys oceans and Indian continent) have been recorded in the SE Plateau (e.g., Deng et al., 2014; Xu et al., 2018), it is highly likely that subducted component of geochemical enrichment must exist in the mantle source region. In the spider diagram (Fig. 5b), alkali basalts in the Maguan area show higher LILE (e.g., Rb, Ba, Pb) and P concentrations, lower Ti contents than OIB. Therefore, mantle metasomatism relating to subducted materials needs consideration. Ba and Pb, as fluid-mobile elements, are regarded as effective indicators for fluid-reaction process (e.g., Bebout et al., 2013) while enrichment of Nb, Th, La, Ce and Nd in the mantle is due to the input of subducted sediment-derived melts (e.g., Castillo and Newhall, 2004). In contrast to Eocene-Oligocene mantle-derived potassic magmas in Western Yunnan, the Maguan alkali basalts have varying higher Ce/Pb (10.63-32.51) and Nb/Y (1.80-2.68), but relatively lower Ba/Y and Ba/Th (Fig. 9). While slab-derived fluids may be important for mantle sources of West Yunnan potassic magmas (e.g., Wang et al., 2001; Guo et al., 2005), slab-derived melt must be important as a metasomatic agent in explaining the varying high Ce/Pb and Nb/Y of the alkali basalts in the Maguan area.

As aforementioned, the Maguan alkali basalts have light Mg isotope compositions (δ^{26}Mg, -0.40--0.60 ‰) that are distinct from global oceanic basalts (δ^{26}Mg = -0.26 ± 0.07‰, Teng et al., 2010) and DMM (δ^{26}Mg = -0.25 ± 0.04‰, Teng et al., 2010). In the magmatic process, ilmenite [(Fe, Mg)TiO_3] tends to have high Ti contents and light Mg isotope composition (Sedaghatpour et al., 2013), while chromite [(Fe, Mg)(Al, Cr)$_2O_4$] presents high Cr and heavy Mg isotopic compositions (Su et al., 2019). As MgO contents may reach up to 8 wt.% in ilmenite (e.g., Papike et al., 1998) and >10 wt.% in chromite (e.g., Xiao et al., 2016), the fractionation of ilmenite and chromite thus has the potential to modify bulk-rock Mg isotope compositions. Nevertheless, the Maguan alkali basalts do not show any bulk-rock Cr-δ^{26}Mg and TiO_2-δ^{26}Mg correlation (Fig. 10), excluding the effect of ilmenite and chromite crystallization on bulk-rock Mg isotope compositions.

It is worth noting that the contribution of recycled oceanic silicate crust should have minimal influence on Mg isotopic compositions of the mantle source because of the overwhelming difference of Mg contents (Table A.3). Besides, as shown in Fig. 6,11, the basaltic samples show lighter δ^{26}Mg ratios than oceanic silicate crust (-0.336‰ for marine sediment and 0.21‰ for altered oceanic basalt, Hu et al., 2017; Ramos et al., 2020). Thus, the contributions of recycled oceanic silicate crust in the mantle source cannot well account for the light Mg isotopic compositions of the Maguan basalts. Apart from the light Mg isotopic compositions, the alkali basalts in the Maguan area have relatively high CaO/Al_2O_3 (0.54-0.68), low Hf/Hf* (0.52-0.89) and Ti/Ti* (0.56-0.92) values (Fig. 11), similar to Cenozoic basalts in Tengchong and Eastern China whose mantle sources have been enriched by recycled carbonates (e.g., Huang and Xiao, 2016; Li et al., 2017; Tian et al., 2018). Importantly, studies have shown that carbonate-rich melt has low TiO_2, HFSEs, Hf/Hf*, Ti/Ti* and δ^{26}Mg (< -1.11 ‰, chiefly), but high CaO/Al_2O_3 and ^{87}Sr/^{86}Sr (> 0.709, mostly) (e.g., Hoernle et al., 2002; Huang and Xiao, 2016). The ratios of Hf/Hf* and Ti/Ti* in the Maguan basalts are lower than those in OIB. And they have a positive relationship with the light Mg isotopic ratios, which are well-plotted along the trend from OIB towards carbonates, but away from the OIB-oceanic silicate crust array (Fig. 11b-c). Compared with DMM, the Maguan basalts show relatively higher ^{87}Sr/^{86}Sr ratios and lighter δ^{26}Mg values, which are similar to Cenozoic basalts in Eastern China (Fig. 6b). According to the Sr-Mg isotope mixing model, they are plotted from DMM towards carbonates, but away from the oceanic silicate crust-DMM mixing arrays (Fig. 6b). We can thus conclude that the asthenospheric mantle beneath the Maguan area had been replenished by carbonate-rich metasomatic agents before the late Miocene.

Carbonates are mainly occurred as calcite [$CaCO_3$] and dolomite [$CaMg(CO_3)_2$] in sediments and hydrothermally altered oceanic crust (e.g., Fantle and Higgins, 2014). However, we need to consider two basic facts here: (1) calcite is not stable under high pressure that cannot exist in the depth of asthenospheric mantle. (2) As Mg is a major element in DMM, but a trace element in calcite, even if calcite were involved, it will have no detectable effect on Mg isotope compositions of DMM. During the subduction process, calcite reacts with silicate to form dolomite, which keeps stable at 2-4 GPa. And dolomite breaks down to magnesite and aragonite at a greater depth (>4 GPa) (e.g., Dasgupta and Hirschmann, 2006). Constrained by geophysical studies (Hu et al., 2015), southeastern Yunnan, where the Maguan area is located, has a 140-180 km thick lithosphere (>4 GPa), thus dolomite would dissociate into magnesite and aragonite in the deep asthenosphere. Besides, seismic tomographic images have reached a consensus that a high-velocity anomaly residing in the mantle transition zone (MTZ, 410-660 km) throughout the SE Plateau is likely to be the remnants of subducted plate, and a ubiquitous low-velocity layer overlaying atop the MTZ is likely associated with slab-derived volatiles where the metasomatism of asthenosphere takes place (e.g., Li et al., 2008; Xu et al., 2018). Therefore, the involvement of magnesite and aragonite, nor dolomite, are more likely to be responsible for the light Mg isotopic compositions of the Maguan alkali basalts. In the geochemical characteristics, aragonite and magnesite are characterized by low HFSE concentrations, high $^{87}Sr/^{86}Sr$ ratios (mode value: 0.7088 and 0.7164, respectively) and low $\delta^{26}Mg$ values (average value: -3.65 and -1.11, respectively) (Table A.3; Liu et al., 2015; Huang and Xiao, 2016). In the plots of Hf/Hf* vs. $\delta^{26}Mg$ (Fig. 11b) and Ti/Ti* vs. $\delta^{26}Mg$ (Fig. 11c), the studied basalts are predominantly situated between the mixing curves of DMM-magnesite and DMM-aragonite. And according to the chemical formulae and the principle of Ca^{2+}-Sr^{2+} isomorphism, the contents of Sr and MgO are the effective indicators to discriminate aragonite and magnesite. The quantitative mixing model of Sr-Mg isotopes also suggests that the mixture of aragonite and magnesite is responsible for the light Mg but relatively depleted Sr isotopic compositions of the Maguan alkali basalts (Fig. 6b). As magnesite and aragonite indeed exist in the deeper mantle evidenced by high P-T experimental petrology (>4 GPa, Dasgupta and Hirschmann, 2006) and diamond inclusions

(Wang et al., 1996), we therefore conclude that the recycled carbonates recorded by the Maguan alkali basalts are dominant by magnesite and aragonite.

5.4. Geodynamics of subduction-related metasomatism

Deep carbon recycling is forced by subduction systems (down) and mantle-derived magmatism (up), which is responsible for light-δ^{26}Mg type refertilized mantle (e.g., Liu et al., 2015; Huang and Xiao., 2016; Li et al., 2017). In the broad region at the southeastern margin of the Tibetan Plateau, several subduction events have been recorded by subducted slabs of the Tethys seafloor subduction, Paleo-Pacific seafloor subduction and Indian oceanic/continental subduction (e.g., Deng et al., 2014, 2018; Zhao et al., 2018), which have been invoked to illustrate the mantle metasomatism beneath southeast Tibetan Plateau (e.g., Guo et al., 2005; Tian et al., 2017; Tian et al., 2018). Deep mantle beneath North China and the South China Sea was proposed to have been enriched by Paleo-Pacific slab (e.g., Huang and Xiao, 2016; Li et al., 2017). However, with a high spatial resolution on mantle tomography, the Paleo-Pacific slab has been recognized to be stagnant in the mantle transition zone beneath eastern China up to ~110°E at the latitude of ~ 23°N (Liu et al., 2017), yet the Maguan area is located further west (~104° E). Besides, lithospheric mantle of the North China craton had been destructed by the subducted Paleo-Pacific oceanic slab (<80 km, Niu, 2005), which had not affected the mantle lithosphere of the Yangtze craton (140-180 km, Hu et al., 2015). As the Yangtze craton is situated between the North China craton in the east and the SE Plateau in the west, the identified mantle metasomatism beneath the SE Plateau would be unrelated to the Paleo-Pacific seafloor subduction.

Recent tomography studies show that the Indian plate or Burma microplate has subducted beneath Tengchong volcanos (e.g., Zhou and Lei, 2016; Xu et al., 2018) and may be responsible for the Tengchong magmatism (e.g., Zou et al., 2014). In contrast to the alkali basalts in the Maguan area, the contemporaneous Tengchong volcanic rocks show negative anomalies in HFSEs (e.g., Nb, Ta, Ti), lower Ba/Th, Ce/Pb and Nb/Y values, but higher Pb and Th contents, and enriched Sr-Nd isotope compositions (Fig. 5,6a,9). The significant geochemical differences imply that the deep mantle beneath the Maguan area had undergone distinct metasomatism from that beneath Tengchong volcano, which is unlikely replenished by the subducted Indian plate or Burma microplate. Besides, the aforementioned remnants of subducted plate stagnated in the MTZ throughout the SE Plateau cannot result from the subducted continent plate, because of its relatively low density (Xu et al., 2018). Hence, it is unlikely that the subducted Indian plate or Burma microplate may have played any significant role in the petrogenesis of the Maguan alkali basalts.

In the broad region at the southeastern margin of the Tibetan Plateau, there are geological records of Neo-Tethys (since Cretaceous), Paleo-Tethys (Devonian-Triassic) and Proto-Tethys (Late Sinian-Silurian) oceans (e.g., Deng et al., 2014,2018; Nie et al., 2015). Based on the studies on Paleozoic magmatism, the asthenospheric mantle in the broad region had been enriched by Proto-Tethys seafloor subduction prior to ~462 Ma (Nie et al., 2015; Xing et al., 2017). Deng et al. (2018) proposed that the Paleo-Tethys seafloor subducted initially at ~252 Ma, indicating another mantle metasomatism event throughout the SE Plateau. However, it is noteworthy that the studied alkali basalts in the Maguan area show apparent decoupling between incompatible element abundances and depleted Sr-Nd isotope compositions, reflecting recent mantle metasomatism (Wang et al., 2001; Liu et al., 2013). As the mantle source of Eocene-Oligocene potassic magmas in Western Yunnan has been interpreted to be metasomatized as the result of the Proto-Tethys seafloor subduction (e.g., Lu et al., 2013) or by the Paleo-Tethys seafloor subduction (Guo et al., 2005; Flower et al., 2013), the Maguan alkali basalts are distinct from the potassic magmas in Western Yunnan (Fig. 5,6) and have the OIB-like geochemistry, suggesting the asthenospheric mantle metasomatism recorded by the Maguan alkali basalts is more likely caused by the subducted Neo-Tethys slabs rather than old subducted slabs associated with the Paleo-Tethys or Proto-Tethys seafloor subduction. Some studies (Xu et al., 2008; Deng et al., 2014) suggest that the Neo-Tethys slab beneath the SE Plateau broke off in 45-40 Ma. It means that prior to 45-40 Ma, the deep mantle had been modified by the subduction of Neo-Tethys seafloor when portions of the Tethys ocean were equatorial with carbonate deposition and subsequently subducted deep into the mantle source region (e.g., Johnston et al., 2011). Therefore, we infer that the asthenospheric mantle metasomatism beneath the Maguan area is caused by the Neo-Tethys seafloor subduction (Fig.12), which is also supported by Liu et al. (2013) that the enriched mantle already existed beneath the Maguan area in the late Cretaceous.

6. Conclusions

(1) Miocene alkali basalts in the Maguan area occur as small-scale pipes containing mantle xenoliths. The lack of apparent correlation of MgO with Sr-Nd isotopes and the high

Ce/Pb (10.63-32.51) and Nb/U (43.75-52.91) suggest that the melts ascended rapidly without significant crustal contamination. The samples represent variably evolved melts dominated by olivine and clinopyroxene crystallization without plagioclase on the liquidus.

(2) The Maguan alkali basalts show high Th/Yb (2.06-3.34), Nb/Yb (26.27-45.81) and TiO_2/Yb (1.12-1.51). Compared with Eocene-Oligocene mantle-derived potassic melts in Western Yunnan, they have positive Nb-Ta anomalies, resembling the present-day OIB in terms of incompatible element patterns and Sr-Nd isotopes. The basalts are best understood as partial melting of metasomatized asthenosphere.

(3) The alkali basalts show higher LILEs (e.g., Rb, Ba, Pb, and lower Ti than OIB. These signatures plus the high Ce/Pb and Nb/Y, and low Ba/Y and Ba/Th, favor the asthenospheric mantle source being enriched by metasomatism of slab-derived melt. Compared to OIB, the Ti/Ti* (0.56-0.92) and Hf/Hf* (0.52-0.89) ratios are relatively low and proportional to the bulk-rock light Mg isotopes (-0.40--0.60‰), pointing to the potential contribution of carbonate as a component of the metasomatic agent. Constrained by the tomography studies and the Sr-Mg isotope mixing model, magnesite associated with aragonite are suggested to be the primary carbonate minerals contributing to the metasomatic agent, which are likely to be caused by the Neo-Tethys seafloor subduction in southeastern Tibetan Plateau prior to the late Miocene.

Acknowledgments

This research was supported by the Second Tibetan Plateau Scientific Expedition and Research (STEP) program (grant 2019QZKK0702), the National Key Research and Development Project of China (grant 2016YFC0600304), the Natural Science Foundation of China (41802058), the 111 Project of the Ministry of Science and Technology of China (B18048). We appreciate Di Zhang, Hong Qin, and Wuhan Sample Solution Analytical Technology Company for lab assistance, Hongwei Ji, Xuejing Tu, Ningyuan Qi, and Chen Li for help during fieldwork and sample analysis. We do thank anonymous reviewers for revising and improving the paper and Editor Xian-Hua Li for editorial handling.

References

Allègre, C.J., Minster, J.F., 1978. Quantitative models of trace element behavior in magmatic processes. Earth and Planetary Science Letters 38, 1-25.

Baudouin, C., France, L., Boulanger, M., Dalou, C., Devidal, J.-L., 2020. Trace element partitioning between clinopyroxene and alkaline magmas: parametrization and role of M1 site on HREE enrichment in clinopyroxenes. Contributions to Mineralogy and Petrology 175, 42.

Bebout, G.E., Agard, P., Kobayashi, K., Moriguti, T., Nakamura, E., 2013. Devolatilization history and trace element mobility in deeply subducted sedimentary rocks: Evidence from Western Alps HP/UHP suites. Chemical Geology 342(2), 1-20.

Boynton, W.V., 1984. Cosmochemistry of the Rare Earth Elements: Meteorite Studies. Developments in Geochemistry 2, 63-114.

Castillo, P.R., Newhall, C.G., 2004. Geochemical constraints on possible subduction components in lavas of Mayon and Taal volcanoes, southern Luzon, Philippines. Journal of Petrology 45, 1089–1108.

Chen, F., Satir, M., Ji, J., Zhong, D., 2002. Nd–Sr–Pb isotopes of Tengchong Cenozoic volcanic rocks from western Yunnan, China: evidence for an enriched-mantle source. Journal of Asian Earth Sciences 21(1), 39-45.

Chung, S.L., Lee, T.Y., Lo, C.H., Wang, P.L., Chen, C.Y., Yem, N.T., Hoa, T.T., Wu, G.-Y., 1997. Intraplate extension prior to continental extrusion along the Ailao Shan-Red River shear zone. Geology 25(4), 311-314.

Chung, S.L., Chu, M.-F., Zhang, Y., Xie, Y., Lo, C.-H., Lee, T.-Y., Lan, C.-Y., Li, X., Zhang, Q., Wang, Y., 2005. Tibetan tectonic evolution inferred from spatial and temporal variations in post-collisional magmatism. Earth-Science Reviews 68, 173-196.

Dasgupta, R., Hirschmann, M.M., 2006. Melting in the Earth's deep upper mantle caused by carbon dioxide. Nature 440, 659-662.

Deng, J., Wang, Q., Li, G., Santosh, M., 2014. Cenozoic tectono-magmatic and metallogenic processes in the Sanjiang region, southeastern China. Earth-Science Reviews 138, 268-299.

Deng, J., Wang, C., Zi, J.W., Xia, R., Li, Q., 2018. Constraining subduction-collision processes of the Paleo-Tethys along the Changning–Menglian Suture: new zircon U-Pb ages and Sr–Nd–Pb–Hf–O isotopes of the Lincang Batholith. Gondwana Research 62, 75-92.

Ding, L., Kapp, P., Zhong, D., Deng, W., 2003. Cenozoic volcanism in Tibet: Evidence for a transition from oceanic to continental subduction. Journal of Petrology 44(10), 1833-1865.

Ersoy, Y., Helvacı, C., 2010. FC-AFC-FCA and mixing modeler: A Microsoft Excel spreadsheet program for modeling geochemical differentiation of magma by crustal fractionation, crustal assimilation and mixing. Computers & Geosciences 36, 383-390.

Fantle, M.S., Higgins, J., 2014. The effects of diagenesis and dolomitization on Ca and Mg isotopes in marine platform carbonates: Implications for the geochemical cycles of Ca and Mg. Geochimica et Cosmochimica Acta 142, 458-481.

Farmer, G.L., 2007. Continental Basaltic Rocks, in: Holland, H.D., Turekian, K.K. (Eds.), Treatise on Geochemistry. Elsevier-Pergamon., Oxford, pp. 1-39.

Flower, M.F.J., Hoàng, N., Lo, C.-H., Chi, C.T., Cuòng, N.Q., Liu, F.-T., Deng, J.-F., Mo, X.-X., 2013. Potassic magma genesis and the Ailao Shan-Red River fault. Journal of Geodynamics 69, 84-105.

Gilley, L.D., Harrison, T.M., Leloup, P.H., Ryerson, F.J., Lovera, O.M., Wang, J.-H., 2003. Direct dating of left-lateral deformation along the Red River shear zone, China and Vietnam. Journal of Geophysical Research: Solid Earth 108(B2), 2127.

Guo, Z., Hertogen, J., Liu, J., Pasteels, P., Boven, A., Punzalan, L., He, H., Luo, X., Zhang, W., 2005. Potassic magmatism in Western Sichuan and Yunnan Provinces, SE Tibet, China: Petrological and geochemical constraints on petrogenesis. Journal of Petrology 46(1), 33-78.

Hoernle, K., Tilton, G., Bas, M.J.L., Duggen, S., Garbe-Schönberg, D., 2002. Geochemistry of oceanic carbonatites compared with continental carbonatites: mantle recycling of oceanic crustal carbonate. Contributions to Mineralogy and Petrology 142(5), 520-542.

Hofmann, A.W., Jochum, K.P., Seufert, M., White, W.M., 1986. Nb and Pb in oceanic basalts: new constraints on mantle evolution. Earth and Planetary Science Letters 79(1-2), 33-45.

Hu, J., Yang, H., Li, G., Peng, H., 2015. Seismic upper mantle discontinuities beneath Southeast Tibet and geodynamic implications. Gondwana Research 28(3), 1032-1047.

Hu, Y., Teng, F.-Z., Plank, T., Huang, K.-J., 2017. Magnesium isotopic composition of subducting marine sediments. Chemical Geology 466, 15-31.

Huang, J., Xiao, Y., 2016. Mg-Sr isotopes of low δ^{26}Mg basalts tracing recycled carbonate species: Implication for the initial melting depth of the carbonated mantle in Eastern China. International Geology Review 58(11), 1350-1362.

Huang, X.-K., 2012. Geochemistry and petrogenesis of Cenozoic basalts in Maguan and Pingbian region, Southeastern Yunan [Ph.D. thesis]. Beijing, China University of Geosciences (Beijing), 113 p. (in Chinese with English abstract)

Huang, X.-L., Niu, Y., Xu, Y.-G., Chen, L.-L., Yang, Q.-J., 2010. Mineralogical and geochemical constraints on the petrogenesis of post-collisional potassic and ultrapotassic rocks from western Yunnan, SW China. Journal of Petrology 51(8), 1617-1654.

Huang, Z., Zhao, D., Wang, L., 2015. P wave tomography and anisotropy beneath Southeast Asia: Insight into mantle dynamics. Journal of Geophysical Research: Solid Earth 120, 5154-5174.

Ito, E., White, W.M., Gòpel, C., 1987. The O, Sr, Nd and Pb isotope geochemistry of MORB. Chemical Geology 62, 157-176.

Jaeger, J.-J., Courtillot, V., Tapponnier, P., 1989. Paleontological view of the ages of the Deccan Traps, the Cretaceous/Tertiary boundary, and the India-Asia collision. Geology 17, 316-319.

Johnston, F.K.B., Turchyn, A.V., Edmonds, M., 2011. Decarbonation efficiency in subduction zones: Implications for warm Cretaceous climates. Earth and Planetary Science Letters 303(1-2), 143-152.

Kuritani, T., Sakuyama, T., Kamada, N., Yokoyama, T., Nakagawa, M., 2017. Fluid-fluxed melting of mantle versus decompression melting of hydrous mantle plume as the cause of intraplate magmatism over a stagnant slab: Implications from Fukue Volcano Group, SW Japan. Lithos 282-283, 98–110.

Li, C., Hilst, R.D., Meltzer, A.S., Engdahl, E.R., 2008. Subduction of the Indian lithosphere beneath the Tibetan Plateau and Burma. Earth and Planetary Science Letters 274(1), 157-168.

Li, M., Zhang, S., Wang, F., Wu, T., Qian, W., 2016. Crustal and upper-mantle structure of the southeastern Tibetan Plateau from joint analysis of surface wave dispersion and receiver functions. Journal of Asian Earth Sciences 117, 52-63.

Li, R., 2009. Mineralogical Study on the Clinopyroxene Megacrysts in the Cenozoic Basalt from Maguan Yunnan province [Master thesis]. Beijing, China University of Geosciences (Beijing), 39 p. (in Chinese with English abstract)

Li, S.-G., Yang, W., Ke, S., Meng, X.-N., Tian, H.-C., Xu, L.-J., He, Y.-S., Huang, J., Wang, X.-C, Xia, Q.-K., Sun, W.-D., Yang, X.-Y., Ren, Z.-Y., Wei, H.-Q., Liu, Y.-S., Meng, F.-C., Yan, J., 2017. Deep carbon cycles constrained by a large-scale mantle Mg isotope anomaly in eastern China. National Science Review 4, 111-120.

Li, X., Liu, J.-Q., 2012. A study on the geochemical characteristics and petrogenesis of Holocene volcanic rocks in Tengchong volcanic eruption field, Yunnan Province, SW China. Acta Petrologica Sinica 28(5), 1507-1517. (in Chinese with English abstract)

Liu, C.-Z., Wu, F.-Y., Sun, J., Chu, Z.-Y., Yu, X.-Y., 2013. Petrology, geochemistry and Re-Os isotopes of peridotite xenolith from Maguan, Yunnan Province: Implications for the Cenozoic mantle replacement in southwestern China. Lithos 168-169(2), 1-14.

Liu, D., Zhao, Z., Zhu, D.-C., Niu, Y., Widom, E., Teng, F.-Z., DePaolo, D.J., Ke, S., Xu, J.-F., Wang, Q., Mo, X.-X., 2015. Identifying mantle carbonatite metasomatism through Os–Sr–Mg isotopes in Tibetan ultrapotassic rocks. Earth and Planetary Science Letters 430, 458-469.

Liu, S.-A., Wang, Z.-Z., Yang, C., Li, S.-G., Ke, S., 2020. Mg and Zn Isotope Evidence for Two Types of Mantle Metasomatism and Deep Recycling of Magnesium Carbonates. Journal of Geophysical Research: Solid Earth 125(11), e2020JB020684.

Liu, X., Zhao, D., Li, S., Wei, W., 2017. Age of the subducting Pacific slab beneath East Asia and its geodynamic implications. Earth and Planetary Science Letters 464, 166-174.

Lu, Y.-J., Kerrich, R., McCuaig, T.C., Li, Z.-X., Hart, C.J.R., Cawood, P.A., Hou, Z.-Q., Bagas, L., Cliff, J., Belousova, E.A., Tang, S.H., 2013. Geochemical, Sr-Nd-Pb, and zircon Hf-O isotopic compositions of Eocene-Oligocene shoshonitic and potassic adakite-like felsic intrusions in western Yunnan, SW China: petrogenesis and tectonic implications. Journal of Petrology 54(7), 1309-1348.

Mo, X., Zhao, Z., Deng, J., Flower, M., Yu, X., Luo, Z., Li, Y., Zhou, S., Dong, G., Zhu, D., Wang, L., 2006. Petrology and geochemistry of postcollisional volcanic rocks from the Tibetan plateau: Implications for lithosphere heterogeneity and collision-induced asthenospheric mantle flow. Geological Society of America special paper 409, 507-530.

McDonough, W.F., Sun, S.-S., 1995. The composition of the Earth. Chemical Geology 120, 223-253.

Nie, X., Feng, Q., Qian, X., Wang, Y., 2015. Magmatic record of Prototethyan evolution in SW Yunnan, China: Geochemical, zircon U-Pb geochronological and Lu-Hf isotopic evidence from the Huimin metavolcanic rocks in the southern Lancangjiang zone. Gondwana Research 28, 757-768.

Niu, Y.L., 2005. Generation and evolution of basaltic magmas: Some basic concepts and a hypothesis for the origin of the Mesozoic-Cenozoic volcanism in eastern China. Geological Journal of China Universities 11, 9-46.

Niu, Y., 2021. Lithosphere thickness controls the extent of mantle melting, depth of melt extraction and basalt compositions in all tectonic settings on Earth - A review and new perspectives. Earth-Science Reviews 217, 103614.

O'Reilly, S.Y., Griffin, W.L., 2011. Rates of magma ascent: Constraints from mantle-derived xenoliths, in: Dosseto, A., Turner, S.P., Orman, J.A.V. (Eds.), Timescales of Magmatic Processes: From Core to Atmosphere. Oxford., UK, Blackwell, pp. 116-124.

Papike, J.J., Ryder, G., Shearer, C.K., 1998. Lunar samples. Reviews in Mineralogy and Geochemistry 36(1), 1-234.

Pearce, J.A., 1996. A user's guide to basalt discrimination diagrams, in: Wynam, D.A. (Ed.), Trace Element Geochemistry of Volcanic Rocks: Applications for Massive Sulphide Exploration. Geological Association of Canada., Short Course Notes 12, 79-113.

Pearce, J.A., 2008. Geochemical fingerprinting of oceanic basalts with applications to ophiolite classification and the search for Archean oceanic crust. Lithos 100(1), 14-48.

Ramos, D.P.S., Coogan, L.A., Murphy, J.G., Higgins, J.A., 2020. Low-temperature oceanic crust alteration and the isotopic budgets of potassium and magnesium in seawater. Earth and Planetary Science Letters 541, 116290.

Rowley, D.B., 1996. Age of initiation of collision between India and Asia: A review of stratigraphic data. Earth and Planetary Science Letters 145, 1-13.

Sedaghatpour, F., Teng, F.-Z., Liu, Y., Sears, D.W.G., Taylor, L.A., 2013. Magnesium isotopic composition of the Moon. Geochimica et Cosmochimica Acta 120, 1-16.

Su, B.-S., Hu, Y., Teng, F.-Z., Xiao, Y., Zhang, H.-F., Sun, Y., Bai, Y., Zhu, B., Zhou, X.-H., Ying, J.-F., 2019. Light Mg isotopes in mantle-derived lavas caused by chromite crystallization, instead of carbonatite metasomatism. Earth and Planetary Science Letters 522, 79-86.

Sun, P., Niu, Y.L., Guo, P.Y., Cui, H.X., Ye, L., Liu, J.J., 2018. The evolution and ascent paths of mantle xenolith-bearing magma: Observations and insights from Cenozoic basalts in Southeast China. Lithos 310-311, 171-181.

Sun, S.S., McDonough, W.F., 1989. Chemical and isotopic systematics of oceanic basalts: implications for mantle composition and processes. Geological Society London Special Publications 42(1), 313-345.

Tapponnier, P., Lacassin, R., Leloup, P.H., Schärer, U., Zhong, D., Wu, H., Liu, X., Ji, S., Zhang, L., Zhong, J., 1990. The Ailao Shan/Red River metamorphic belt: Tertiary left-lateral shear between Indochina and South China. Nature 343, 431-437.

Taylor, S.R., 1964. Abundance of chemical elements in the continental crust: a new table. Geochimica et Cosmochimica Acta 28, 1273-1285.

Teng, F.-Z., Li, W.-Y., Ke, S., Marty, B., Dauphas, N., Huang, S., Wu, F.-Y., Pourmand, A., 2010. Magnesium isotopic composition of the Earth and chondrites. Geochimica et Cosmochimica Acta 74, 4150-4166.

Teng, F.-Z., Li, W.-Y., Ke, S., Yang, W., Liu, S.-A., Sedaghatpour, F., Wang, S.-J., Huang, K.-J., Hu, Y., Ling, M.-X., Xiao, Y., Liu, X.-M., Li, X.-W., Gu, H.-O., Sio, C.K., Wallace, D.A., Su, B.-X., Zhao, L., Chamberlin, J., Harrington, M., Brewer, A., 2015. Magnesium Isotopic Compositions of International Geological Reference Materials. Geostandards and Geoanalytical Research 39(3), 329-339.

Tian, H.-C., Yang, W., Li, S.-G, Ke, S., Duan, X.-Z., 2018. Low δ^{26}Mg volcanic rocks of Tengchong in Southwestern China: A deep carbon cycle induced by supercritical liquids. Geochimica et Cosmochimica Acta 240, 191-219.

Tian, S.-H., Yang, Z.-S., Hou, Z.-Q., Mo, X.-X., Hu, W.-J., Zhao, Y., Zhao, X.-Y., 2017. Subduction of the Indian lower crust beneath southern Tibet revealed by the post-collisional potassic and ultrapotassic rocks in SW Tibet. Gondwana Research 41, 29-50.

Wang, A., Pasteris, J.D., Meyer, H.O.A., Dele-Duboi, M.L., 1996. Magnesite-bearing inclusion assemblage in natural diamond. Earth and Planetary Science Letters 141, 293-306.

Wang, J.-H., Yin, A., Harrison, T.M., Grove, M., Zhang, Y.-Q., Xie, G.-H., 2001. A tectonic model for Cenozoic igneous activities in the eastern Indo–Asian collision zone. Earth and Planetary Science Letters 188(1), 123-133.

Wei. Q.-R., Wang, J.-H., 2004. Geochemical characteristics of Cenozoic basaltic high-K volcanic rocks from Maguan area, eastern Tibet. Chinese Journal of Geochemistry 23(1), 57-64.

White, W.M., 2010. Oceanic Island Basalts and Mantle Plumes: The Geochemical Perspective. The Annual Review of Earth and Planetary Sciences 38, 133-160.

Xia, P., Xu, Y.-G., 2005. Domains and enrichment mechanism of the lithospheric mantle in western Yunnan: A comparative study on two types of Cenozoic ultrapotassic rocks. Science in China Ser. D Earth Science 49(3), 326-337.

Xiao, Y., Teng, F.-Z., Su, B.-X., Hu, Y., Zhou, M.-F., Zhu, B., Shi, R.-D., Huang, Q.-S., Gong, X.-H., He, Y.-S., 2016. Iron and magnesium isotopic constraints on the origin of chemical heterogeneity in podiform chromitite from the Luobusa ophiolite, Tibet. Geochemistry, Geophysics, Geosystems 17(3), 940-953.

Xing, X., Wang, Y., Cawood, P.A., Zhang, Y., 2017. Early Paleozoic accretionary orogenesis along north margin of Gondwana constrained by high-Mg metaigneous rocks, SW Yunnan. International Journal of Earth Sciences 106(5), 1469-1486.

Xu, M., Huang, H., Huang, Z., Wang, P., Wang, L., Xu, M., Mi, N., Li, H., Yu, D., Yuan, X., 2018. Insight into the subducted Indian slab and origin of the Tengchong volcano in SE Tibet from receiver function analysis. Earth and Planetary Science Letters 482, 567-579.

Xu, Y.-G., Lan, J.-B., Yang, Q.-J., Huang, X.-L., Qiu, H.-N., 2008. Eocene break-off of the Neo-Tethyan slab as inferred from intraplate-type mafic dykes in the Gaoligong orogenic belt, eastern Tibet. Chemical Geology 255, 439-453.

Young, E.D., Galy, A., 2004. The isotope geochemistry and cosmochemistry of magnesium. Reviews in Mineralogy and Geochemistry 55(1), 197-230.

Yu, X.-H., Mo, X.-X., Zeng, P.-S., Xiao, X.-N., 2006. A study on the mantle xenoliths in the Cenozoic volcanic rocks from Maguan Area, Yunnan Province. Acta Petrologica Sinica 22(3), 621-630. (in Chinese with English abstract)

Zhang, W., Hu, Z., 2020. Estimation of Isotopic Reference Values for Pure Materials and Geological Reference Materials. Atomic Spectroscopy 41(3), 93-102.

Zhao, J.-H., Li, Q.-W., Liu, H., Wang, W., 2018. Neoproterozoic magmatism in the western and northern margins of the Yangtze Block (South China) controlled by slab subduction and subduction-transform-edge-propagator. Earth-Science Reviews 187, 1-18.

Zhao, Z., Mo, X., Dilek, Y., Niu, Y., DePaolo, D.J., Robinson, P., Zhu, D., Sun, C.G., Dong, G., Zhou, Su., Luo, Z., Hou, Z., 2009. Geochemical and Sr–Nd–Pb–O isotopic compositions of the post-collisional ultrapotassic magmatism in SW Tibet: Petrogenesis and implications for India intra-continental subduction beneath southern Tibet. Lithos 113(1), 190-212.

Zhou, M.F., Robinson, P.-T., Wang, C.Y., Zhao, J.-H., Yan, D.-P., Gao, J.-F., Malpas, J., 2012. Heterogeneous mantle source and magma differentiation of quaternary arc-like volcanic rocks from Tengchong, SE margin of the Tibetan Plateau. Contributions to Mineralogy and Petrology 163(5), 841-860.

Zhou, Z., Lei, J., 2016. Pn anisotropic tomography and mantle dynamics beneath China. Physics of the Earth and Planetary Interiors 257, 193-204.

Zindler, A., Hart, S.R., 1986. Chemical geodynamics. Annual Review of Earth and Planetary Sciences 14, 493-571.

Zou, H., Fan, Q., Schmitt, A. K., Sui, J., 2010. U-Th dating of zircons from Holocene potassic andesites (Maanshan volcano, Tengchong, SE Tibetan Plateau) by depth profiling: Time scales and nature of magma storage. Lithos 118(1), 202-210.

Zou, H., Shen, C.-C., Fan, Q., Lin, K., 2014. U-series disequilibrium in young Tengchong volcanics: Recycling of mature clay sediments or mudstones into the SE Tibetan mantle. Lithos 192-195, 132-141.

Figure captions

Figure 1. (a) Topography and tectonic sketch throughout southeastern Tibetan Plateau (after Li et al., 2016), and the major tectonic constituents of the Tibetan Plateau (shown in the inserted plot, after Mo et al., 2006). Also, Cenozoic mantle-derived volcanic activities in the SE Plateau are shown in space and time (in Ma), which are quoted from Wang et al. (2001), Huang et al. (2010), Zou et al. (2010), Huang (2012). SGF – Sagaing Fault, LCF – Lancangjiang Fault, RRF – Red-River Fault, XSHF – Xianshuihe Fault, XJF – Xiaojiang Fault. The main suture belts between the terranes are: I – Xiugou–Maqin; II – Jinshajiang-Ailaoshan; III – Garze–Litang; IV – Longmuco-Shuanggou-Lancangjiang; V – Bangongco–Nujiang; VI - Indus–Yarlung Tsangpo. (b) Geological map of the Maguan area and sample locations.

Figure 2. (a) Outcrop of Haozibа pipe in the Maguan area, where explosive breccias are overlain by basaltic lavas. (b-c) Photomicrographs of reprehensive basaltic sample from the Maguan area (d) Backscattered electron image of representative basaltic sample. Abbreviations of minerals are: Ol – Olivine; Cpx – Clinopyroxene; Pl – Plagioclase.

Figure 3. Harker diagrams showing the variation of selected major oxides (a-d), trace elements (e), trace element ratios (f-h), and $^{87}Sr/^{86}Sr$ ratios (i) against MgO in Cenozoic basaltic magmas from the Maguan area and its adjacent region. The fields of oceanic basalts are modified from Hofmann et al. (1986). The sources of literature data: Miocene basalts in the Maguan area (Wang et al., 2001; Wei and Wang, 2004; Xia and Xu, 2005; Flower et al., 2013; Huang, 2012; Liu et al., 2020), Eocene-Oligocene mantle-derived potassic magmas in Western Yunnan (Wang et al., 2001; Xia and Xu, 2005; Guo et al., 2005; Huang et al., 2010; Liu et al., 2020), and Tengchong

mafic volcanic suites (Chen et al., 2002; Li and Liu, 2012; Zhou et al., 2012; Zou et al., 2014; Tian et al., 2018). To avoid the effects of significant magma differentiation and crustal contamination, the aforementioned literature data are plotted with SiO_2 <55 wt.% and MgO >5 wt.% on an anhydrous basis.

Figure 4. Basalt classification using Zr/TiO_2 vs. Nb/Y (modified from Pearce, 1996). Miocene basalts in the Maguan area plot in the field of alkali basalt with the highest Nb/Y ratios among Eocene-Oligocene mantle-derived potassic magmas in Western Yunnan and Tengchong mafic volcanic suites. The sources of literature data are the same as those in Fig. 3.

Figure 5. (a) Chondrite-normalized (Boyton, 1984) REE patterns and (b) primitive mantle-normalized (McDonough and Sun, 1995) spider diagram for Cenozoic basaltic magmas from the Maguan area and its adjacent region. The average OIB, E-MORB and N-MORB (Sun and McDonough, 1989) are plotted for comparison. Except for Cenozoic basalts in Eastern China are quoted from Li et al., 2017, the rest of literature data on the Cenozoic magmas are as those in Fig. 3.

Figure 6. (a) Sr-Nd isotopes of Cenozoic basaltic magmas from the Maguan area and its adjacent region. Both EM I and EM II endmembers are from Zinder and Hart (1986). MORB and OIB fields are after Ito et al. (1987) and White (2010), respectively. The data of peridotite xenoliths hosted in the Maguan basalts are from Huang (2012). (b) Plot on $\delta^{26}Mg_{DSM3}$ against $^{87}Sr/^{86}Sr$. The small solid circles in the mixing curves represent an increment of 10%. Error bars of Mg isotopic ratios represent two standard deviations. The endmember parameters for Sr-Mg isotope mixing model calculations are listed in Table A.3. The OIB data are sourced from Teng et al. (2010) for Mg isotopes and Sun and McDonough (1989) for the rest data. AOB is the abbreviation of altered oceanic basalt. The data sources of the Cenozoic magmas are as those in Fig. 3,5.

Figure 7. Correlations between (a) $(La/Sm)_N$ vs. Sr and (b) $(La/Sm)_N$ vs. ΣLREE, to evaluate the effect of partial melting and fractional crystallization processes on the compositional variations in the Maguan basalts. The fractional crystallization curves of olivine and clinopyroxene are

based on the numerical simulation by Ersoy and Helvacı (2010). With the highest MgO content in the studied basalts, Sample LFZ1612 is relatively less evolved and selected as the endmember for fractional crystallization modeling. The small solid circles in the curves represent an increment of 10%. The partial melting trends are modified from Allègre and Minster (1978). The subscript "N" represents normalization by chondrite. The literature data and symbols are the same as those in Fig. 3.

Figure 8. Plots on (a) Th/Yb vs. Nb/Yb and (b) TiO_2/Yb vs. Nb/Yb to distinguish IAB (Island Arc basalt), OIB and MORB (after Pearce, 2008). The rest literature data and symbols are as those in Fig. 3.

Figure 9. Plots on (a) Ce/Pb vs. Ba/Th and (b) Ba/Y vs. Nb/Y (modified from Zhao et al., 2009) to identify the metasomatism type of magma source. The literature data and symbols are as those in Fig. 3.

Figure 10. Correlations between (a) $\delta^{26}Mg_{DSM3}$ vs. TiO_2 and (b) $\delta^{26}Mg_{DSM3}$ vs. Cr, to eliminate the fractional crystallization of ilmenite (after Sedaghatpour et al., 2013) and chromite (Su et al., 2019). The literature data and symbols are as those in Fig. 3.

Figure 11. $\delta^{26}Mg_{DSM3}$ against CaO/Al_2O_3 (a), Hf/Hf* (b) and Ti/Ti* (c), exhibiting an input of carbonate component into the mantle source of Cenozoic alkali basalts in the Maguan area. The solid curves represent the binary mixing trends between DMM and other endmembers, revealing the co-variation correlations defined by Hf/Hf*, Ti/Ti* and Mg isotopes of the Maguan alkali basalts. And the geochemical data of endmembers are given in Table A.3. Error bars on Mg isotopic ratios are two standard deviations. The sources of OIB data are from Sun and McDonough (1989), Teng et al. (2010). Mg isotope data of Cenozoic basalts in Eastern China are from Li et al. (2017). $Hf/Hf^* = Hf_N/(Sm_N{*}Nd_N)^{0.5}$, $Ti/Ti^* = Ti_N/(Nd_N^{-0.055}{*}Sm_N^{0.333}{*}Gd_N^{0.722})$, where subscript "N" represents normalization by primitive mantle.

Figure 12. A schematic cartoon model illustrating the geodynamics of mantle carbonation and the possible mechanisms of Miocene Maguan basalt generation in SE Tibetan Plateau, which is

based on the high-resolution tomography images from Li et al. (2008) and Xu et al. (2018). CMF fault – Churachandpur-Mao fault, CBB – Central Burma basin, NJF – Nujiang fault, RRF – Red River fault, LAB - Lithosphere-Asthenosphere boundary. Heretofore, the mechanism of the Maguan basalt generation is still controversial, which is mainly summarized as the shallower asthenospheric mantle vs mantle plume in origin (Kuritani et al., 2017). The literature sources on the mechanisms of the Maguan basalt generation: the mechanism of asthenosphere upwelling is hypothesized by Wang et al. (2001), which is probably induced by widerspread simultaneous east-west extension over eastern Asia. And the mechanism associated with Hainan mantle plume is supported by the seismic tomography that a plume-like low-velocity zone beneath Hainan Island is imaged to continuously extend to Southeast Asia and the southeastern margin of Tibetan Plateau (e.g., Huang et al., 2015).

Declaration of interest statement

The authors declare that they have no known competing financial interests or personal relationships that could have appeared to influence the work reported in this paper.

Highlights

1. Miocene basalt in Maguan area, SW China was evolved without crustal contamination
2. The Maguan basalt is derived from metasomatized asthenospheric mantle
3. The mantle metasomatism was predominantly caused by deep recycled carbonates.

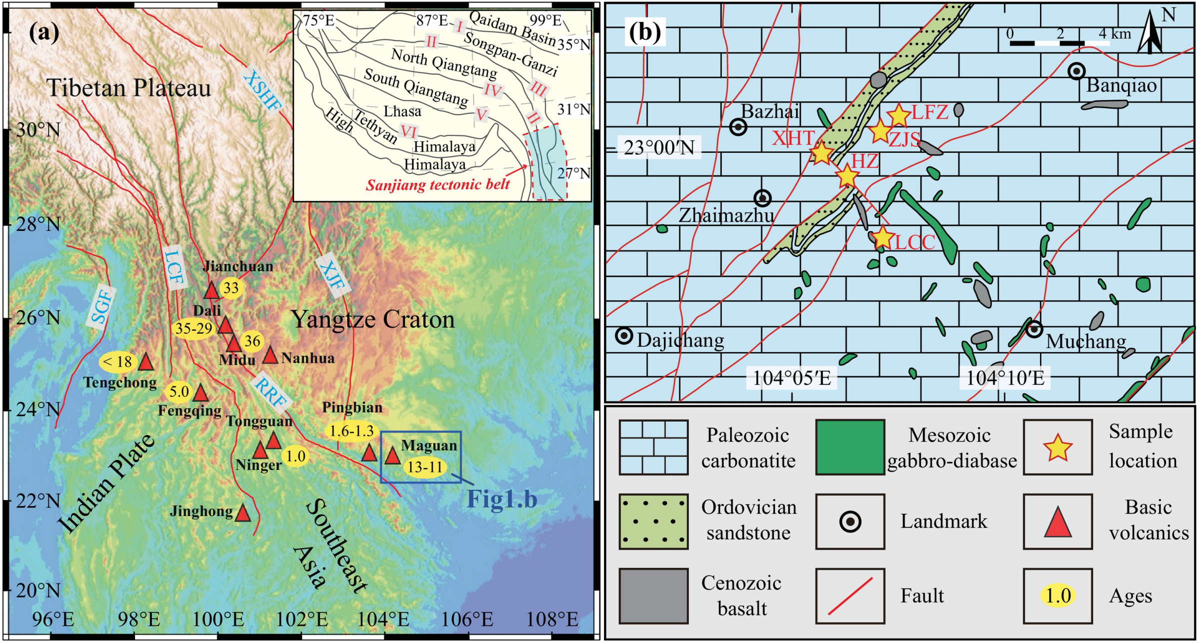
(a)
Tibetan Plateau
XSHF
75°E
87°E
99°E
I
II
Qaidam Basin
35°N
Songpan-Ganzi
North Qiangtang
South Qiangtang
IV
III
31°N
Lhasa
V
II
High
Tethyan
VI
Himalaya
Himalaya
27°N
Sanjiang tectonic belt
30°N
28°N
26°N
24°N
22°N
20°N
LCF
SGF
XJF
RRF
Jianchuan
33
Dali
35-29
36
Midu
Nanhua
Yangtze Craton
< 18
Tengchong
5.0
Fengqing
Tongguan
Ninger
1.0
Pingbian
1.6-1.3
Maguan
13-11
Fig1.b
Indian Plate
Jinghong
Southeast Asia
96°E
98°E
100°E
102°E
104°E
106°E
108°E
(b)
0
2
4 km
N
Banqiao
Bazhai
LFZ
XHT
ZJS
23°00′N
HZ
Zhaimazhu
LCC
Dajichang
Muchang
104°05′E
104°10′E
Paleozoic carbonatite
Mesozoic gabbro-diabase
Sample location
Ordovician sandstone
Landmark
Basic volcanics
Cenozoic basalt
Fault
1.0
Ages

Figure 1

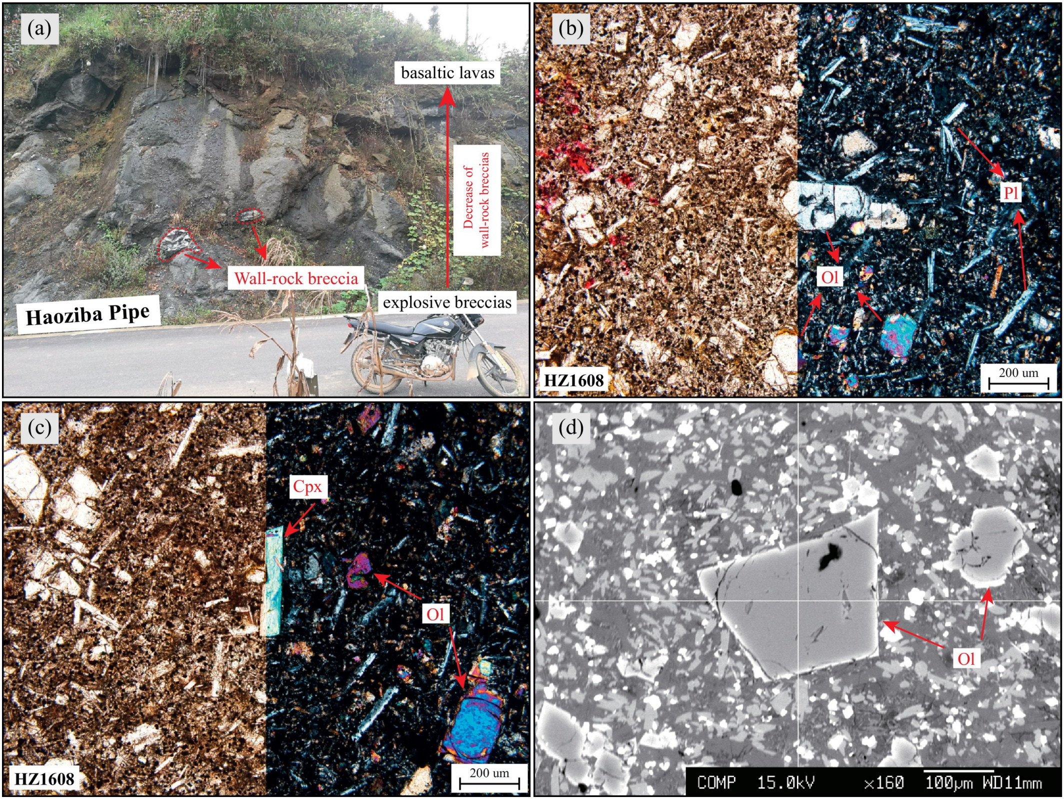
(a)
basaltic lavas
Decrease of wall-rock breccias
Wall-rock breccia
explosive breccias
Haoziba Pipe
(b)
Pl
Ol
HZ1608
200 um
(c)
Cpx
Ol
HZ1608
200 um
(d)
Ol
COMP 15.0kV ×160 100μm WD11mm

Figure 2

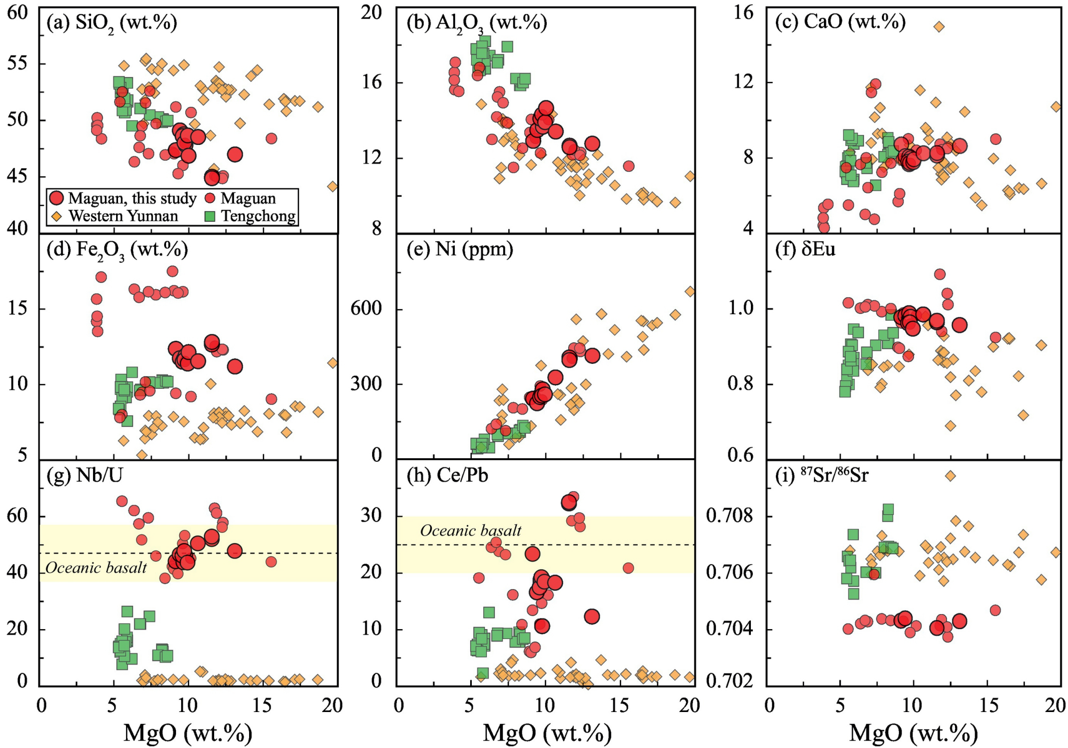
(a) SiO2 (wt.%)
(b) Al2O3 (wt.%)
(c) CaO (wt.%)
(d) Fe2O3 (wt.%)
(e) Ni (ppm)
(f) δEu
(g) Nb/U
(h) Ce/Pb
(i) 87Sr/86Sr
Maguan, this study
Maguan
Western Yunnan
Tengchong
Oceanic basalt
Oceanic basalt
MgO (wt.%)
MgO (wt.%)
MgO (wt.%)

Figure 3

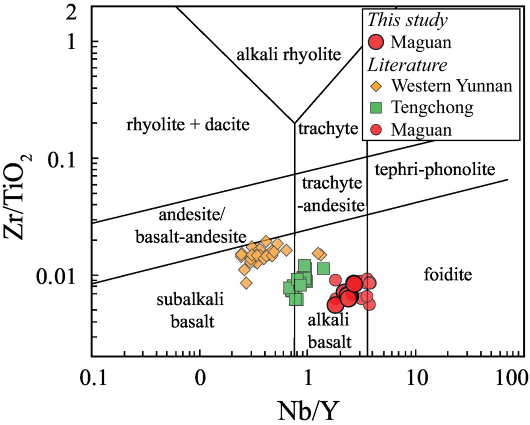

This study
Maguan
Literature
Western Yunnan
Tengchong
Maguan
alkali rhyolite
rhyolite + dacite
trachyte
tephri-phonolite
trachyte
-andesite
andesite/
basalt-andesite
subalkali
basalt
alkali
basalt
foidite
Zr/TiO2
Nb/Y
2
1
0.1
0.01
0.1
0
1
10
100

Figure 4

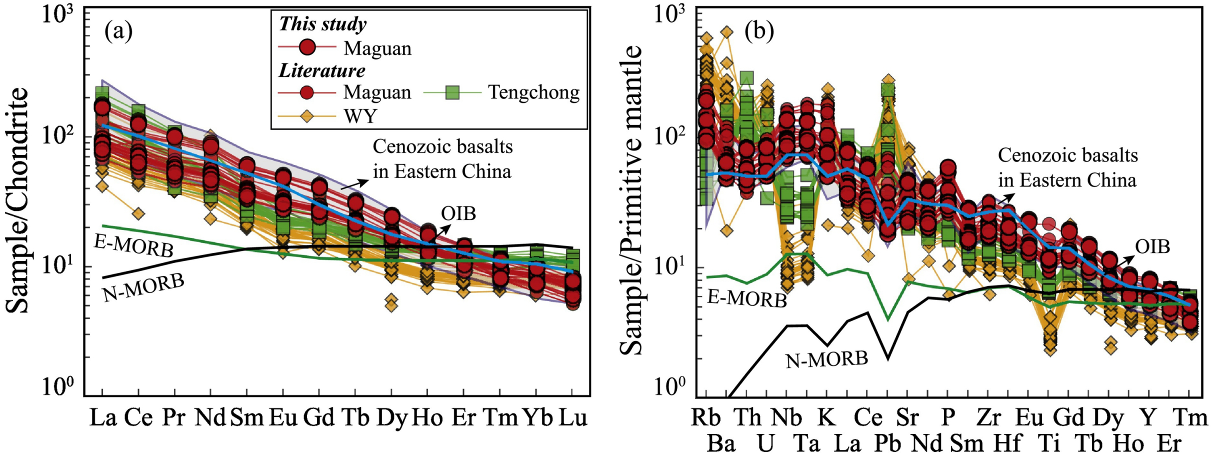

(a)
This study
Maguan
Literature
Maguan
Tengchong
WY
Cenozoic basalts
in Eastern China
OIB
E-MORB
N-MORB
Sample/Chondrite
La Ce Pr Nd Sm Eu Gd Tb Dy Ho Er Tm Yb Lu
(b)
Cenozoic basalts
in Eastern China
OIB
E-MORB
N-MORB
Sample/Primitive mantle
Rb Th Nb K Ce Sr P Zr Eu Gd Dy Y Tm
Ba U Ta La Pb Nd Sm Hf Ti Tb Ho Er

Figure 5

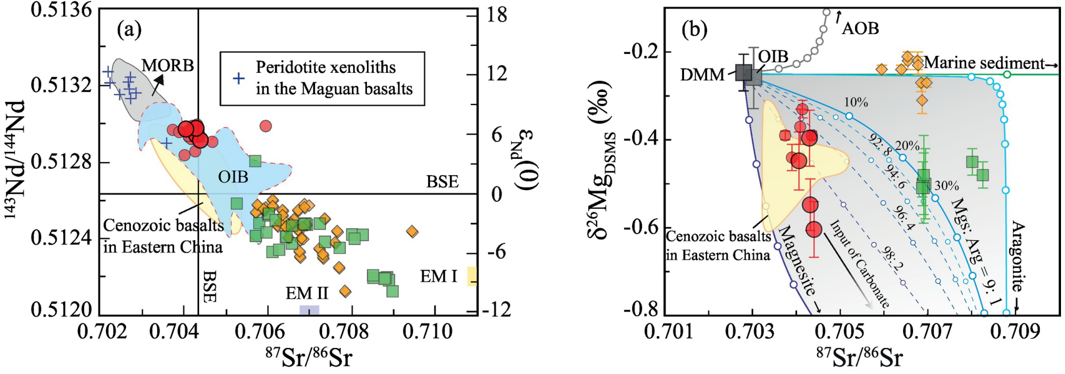
(a)
MORB
Peridotite xenoliths
in the Maguan basalts
OIB
BSE
Cenozoic basalts
in Eastern China
BSE
EM I
EM II
0.5136
0.5132
0.5128
0.5124
0.5120
0.702
0.704
0.706
0.708
0.710
18
12
6
0
-6
-12
$^{143}Nd/^{144}Nd$
$\varepsilon_{Nd}(0)$
$^{87}Sr/^{86}Sr$
(b)
AOB
OIB
DMM
Marine sediment
10%
20%
30%
92: 8
94: 6
96: 4
98: 2
Mgs: Arg = 9: 1
Aragonite
Magnesite
Input of Carbonate
Cenozoic basalts
in Eastern China
-0.2
-0.4
-0.6
-0.8
0.701
0.703
0.705
0.707
0.709
$\delta^{26}Mg_{DSMS}$ (‰)
$^{87}Sr/^{86}Sr$

Figure 6

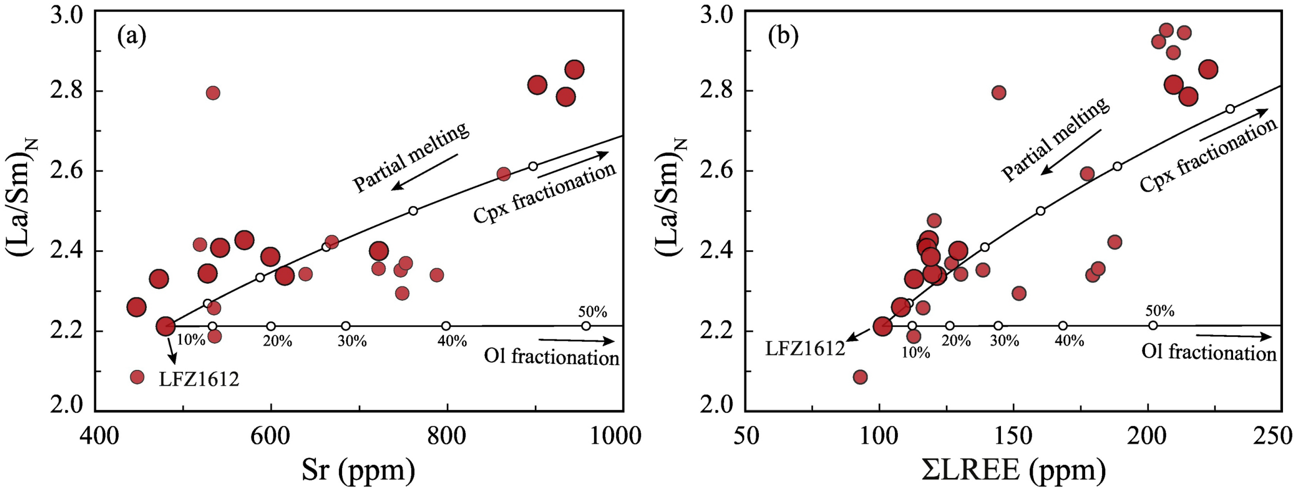

(a)
(La/Sm)N
Sr (ppm)
Partial melting
Cpx fractionation
Ol fractionation
LFZ1612
10%
20%
30%
40%
50%
(b)
ΣLREE (ppm)

Figure 7

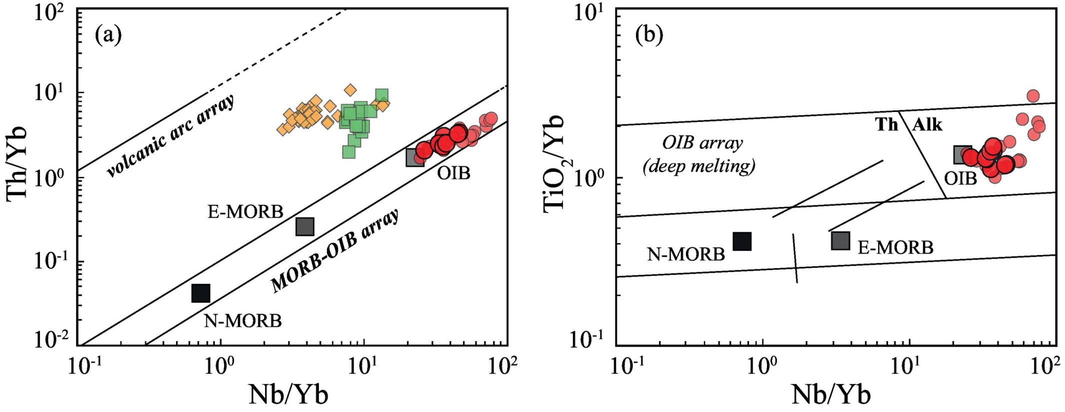

(a)
volcanic arc array
E-MORB
MORB-OIB array
N-MORB
OIB
Th/Yb
Nb/Yb
10^{2}
10^{1}
10^{0}
10^{-1}
10^{-2}
10^{-1}
10^{0}
10^{1}
10^{2}
(b)
OIB array
(deep melting)
Th
Alk
OIB
N-MORB
E-MORB
TiO_2/Yb
Nb/Yb
10^{1}
10^{0}
10^{-1}
10^{-1}
10^{0}
10^{1}
10^{2}

Figure 8

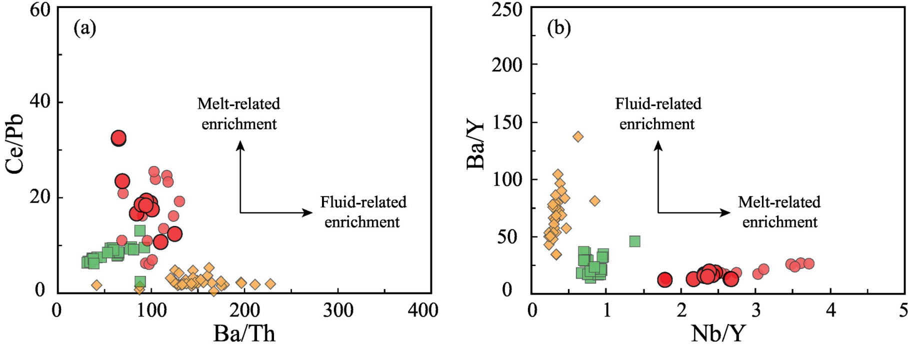

(a)
Ce/Pb
Ba/Th
Melt-related enrichment
Fluid-related enrichment
0
20
40
60
0
100
200
300
400
(b)
Ba/Y
Nb/Y
Fluid-related enrichment
Melt-related enrichment
0
50
100
150
200
250
0
1
2
3
4
5

Figure 9

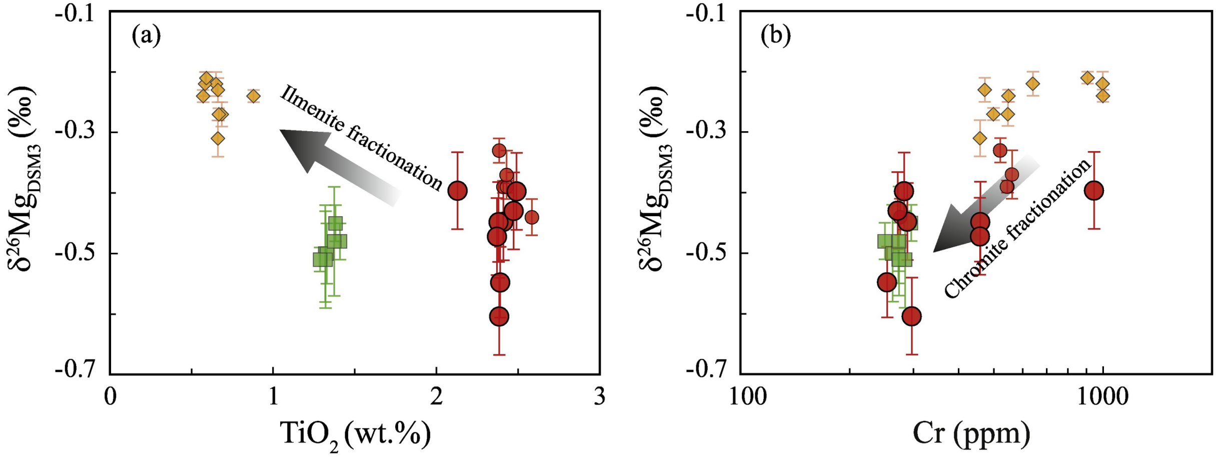
(a)
(b)
Ilmenite fractionation
Chromite fractionation
$\delta^{26}Mg_{DSM3}$ (‰)
-0.1
-0.3
-0.5
-0.7
0
1
2
3
TiO_2 (wt.%)
100
1000
Cr (ppm)

Figure 10

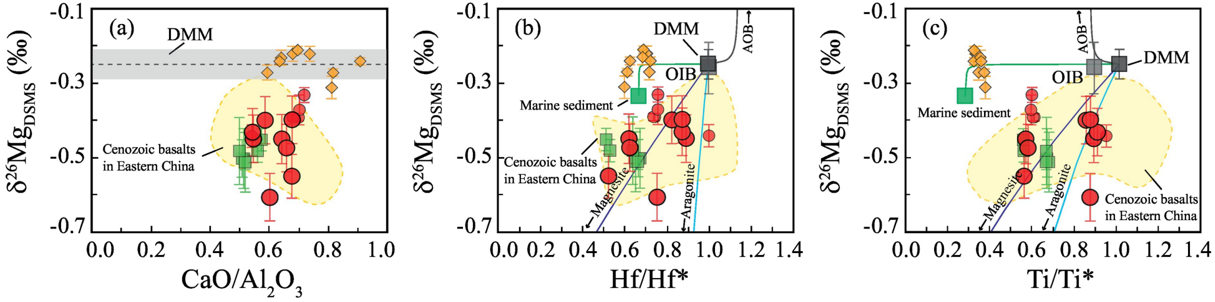
(a)
DMM
Cenozoic basalts
in Eastern China
$\delta^{26}Mg_{DSMS}$ (‰)
CaO/Al$_2$O$_3$
(b)
DMM
OIB
AOB
Marine sediment
Cenozoic basalts
in Eastern China
Magnesite
Aragonite
Hf/Hf*
(c)
DMM
OIB
AOB
Marine sediment
Magnesite
Aragonite
Cenozoic basalts
in Eastern China
Ti/Ti*

Figure 11

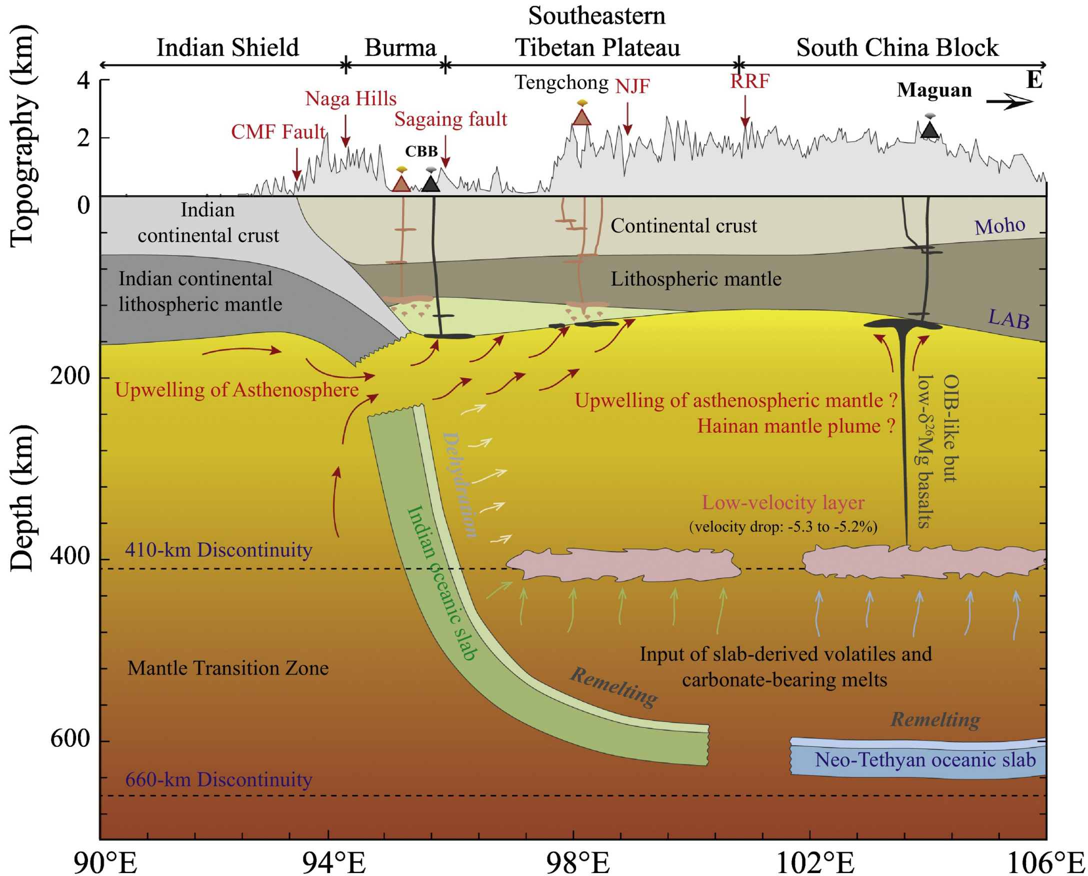

Southeastern Tibetan Plateau
Indian Shield
Burma
South China Block
Topography (km)
4
2
0
E
Naga Hills
CMF Fault
Sagaing fault
CBB
Tengchong
NJF
RRF
Maguan
Indian continental crust
Indian continental lithospheric mantle
Continental crust
Lithospheric mantle
Moho
LAB
Upwelling of Asthenosphere
Upwelling of asthenospheric mantle ?
Hainan mantle plume ?
OIB-like but low-δ26Mg basalts
Dehydration
Indian oceanic slab
Low-velocity layer
(velocity drop: -5.3 to -5.2%)
410-km Discontinuity
Input of slab-derived volatiles and carbonate-bearing melts
Mantle Transition Zone
Remelting
Remelting
Neo-Tethyan oceanic slab
660-km Discontinuity
Depth (km)
200
400
600
90°E
94°E
98°E
102°E
106°E

Figure 12